nature physics

ARTICLES

https://doi.org/10.1038/s41567-022-01651-7

Long-lived phantom helix states in Heisenberg quantum magnets

Paul Niklas Jepsen[1,2], Yoo Kyung 'Eunice' Lee[1,2] ✉, Hanzhen Lin[1,2], Ivana Dimitrova[2,3], Yair Margalit[1,2], Wen Wei Ho[3,4] and Wolfgang Ketterle[1,2]

Exact solutions for quantum many-body systems are rare but provide valuable insights for the description of universal phenomena such as the non-equilibrium dynamics of strongly interacting systems and the characterization of new forms of quantum matter. Recently, specific solutions of the Bethe ansatz equations for integrable spin models were found. They are dubbed phantom Bethe states and can carry macroscopic momentum yet no energy. Here, we show experimentally that there exist special helical spin patterns in anisotropic Heisenberg chains which are long-lived, relaxing only very slowly in dynamics, as a consequence of such states. We use these phantom spin-helix states to directly measure the interaction anisotropy, which has a major contribution from short-range off-site interactions. We also generalize the theoretical description to higher dimensions and other non-integrable systems and find analogous stable spin helices, which should show non-thermalizing dynamics associated with so-called quantum many-body scars. These results have implications for the quantum simulation of spin physics, as well as many-body dynamics.

The dynamics of strongly interacting quantum many-body systems is an active frontier of research. It has broad implications ranging from understanding fundamental phenomena such as quantum thermalization or the lack thereof[1–5] to realizing new forms of matter (for example, time crystals[6,7]) and to controlling entanglement for quantum information processing[8,9]. However, analysing such systems in full is difficult due to their complexity.

A large class of models which allows us to make significant progress is that of integrable systems. These systems feature stable quasiparticles at finite temperatures and occur generally in one spatial dimension. Indeed, a wealth of dynamical phenomena has been uncovered in them, such as generalized quantum thermalization[10] and spin transport belonging to various universality classes such as ballistic, diffusive and even superdiffusive lying in the celebrated Kardar–Parisi–Zhang class, the latter of which was only recently predicted[11–13] and experimentally observed[14].

Another recent development is the theoretical discovery that many integrable models host a special set of many-body eigenstates that are degenerate, that is, so-called phantom Bethe states[15]. These states are composed of multiple quasiparticles which carry momentum but contribute zero energy (relative to the reference 'vacuum' state), akin to ghost particles, hence the term 'phantom'. The existence of such states implies that there are special initial, far-from-equilibrium configurations which do not thermalize to a (generalized) Gibbs ensemble, hence representing an exception to (generalized) quantum thermalization.

An integrable model which is paradigmatic for this behaviour is the spin-1/2 anisotropic Heisenberg model in one dimension, whose Hamiltonian is given by

$$H = J_{xy} \sum_{\langle ij \rangle} [S_i^x S_j^x + S_i^y S_j^y + \Delta S_i^z S_j^z]. \qquad (1)$$

Here, the transverse and longitudinal spin couplings (between neighbouring sites i and j) are J_{xy} and $J_z := J_{xy}\Delta$, respectively, where Δ is the spin-exchange anisotropy. For this model, simple patterns of spins winding in the transverse plane, that is, spin-helix states, share the properties of the phantom Bethe states if their pitch λ or wavevector $Q := 2\pi/\lambda = Q_p$ satisfies the 'phantom condition'

$$\Delta = \cos(Q_p a), \qquad (2)$$

where a is the lattice spacing. These 'phantom helix states' are exact many-body eigenstates of the system and do not decay.

In this work, we utilize our versatile ultracold atom quantum simulator platform with tunable anisotropy[16,17] to search for the phantom helix states in the Heisenberg model (equation (1)). We systematically explore the dynamics of spin-helix states and study their decay as a function of wavevector Q for different fixed anisotropies Δ, finding a non-monotonic decay rate with a pronounced minimum near the expected special value Q_p. This is the signature of the phantom spin-helix state, confirming the theoretical predictions of ref. [15] and providing the first experimental evidence for this novel general feature of integrable systems.

We further investigate whether the phenomenon of phantom spin helices persists beyond integrable systems. We theoretically establish generalizations of the phantom spin-helix states to Heisenberg models of higher dimensions, with higher spin quantum numbers, and for non-cubic lattice geometries. The existence of stable far-from-equilibrium helices in such systems, which are non-integrable in general, leads to genuinely non-thermalizing dynamics associated with so-called quantum many-body scars[18]. We propose an experimental protocol to realize such scarred dynamics with ultracold atoms.

In addition to the fundamental importance of phantom helices for spin physics, the dynamics of phantom helices can be applied as an important tool for quantum simulations of spin physics. Using the phantom condition (equation (2)), we demonstrate how it is now possible to experimentally determine the anisotropy Δ of the Heisenberg model. Our measurements show that the anisotropy

---

[1]Department of Physics and Research Laboratory of Electronics, Massachusetts Institute of Technology, Cambridge, MA, USA. [2]MIT–Harvard Center for Ultracold Atoms, Cambridge, MA, USA. [3]Department of Physics, Harvard University, Cambridge, MA, USA. [4]Department of Physics, Stanford University, Stanford, CA, USA. ✉e-mail: eunlee@mit.edu

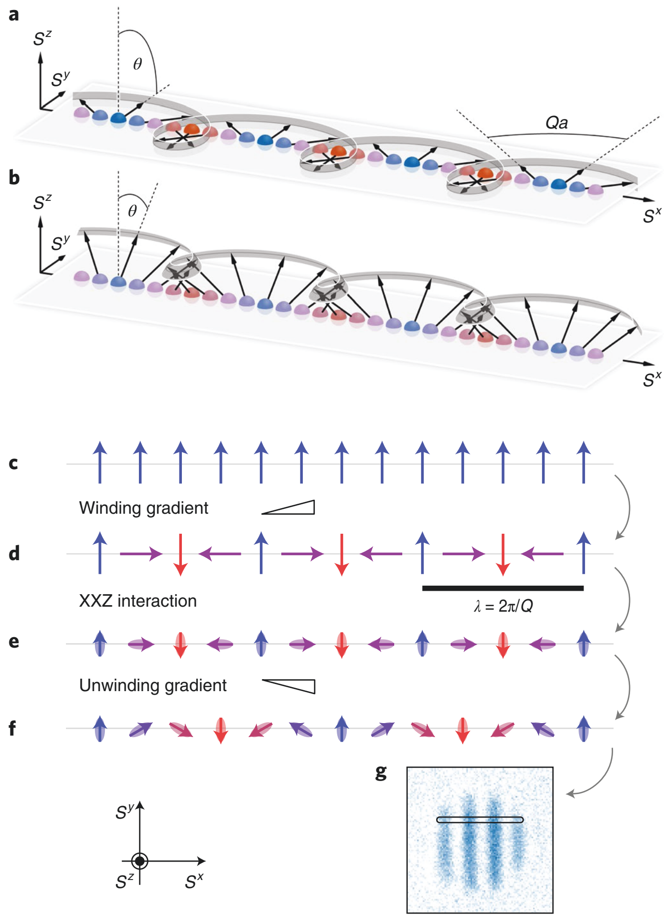

Fig. 1 | Preparation and observation of spin-helix states. a–g, We prepare a transverse spin helix where the spin vector winds within the S^x–S^y plane with $\theta=\pi/2$ (**a**) or with arbitrary polar angle θ (**b**). Black arrows indicate the direction of the spins of the atoms (spheres) aligned along $+S^y$ (blue), $-S^y$ (red) or intermediate directions (purple); grey ribbon is to guide the eye. An initially spin-polarized state in the S^y direction (**c**) is wound into a spin helix with variable wavevector Q using a magnetic field gradient (black triangles). Here, we illustrate a winding of $Qa=\pi/2$ (**d**). This state evolves under the XXZ Heisenberg Hamiltonian (**e**). After unwinding the remaining spin modulation to a resolvable wavevector (**f**), the local S^y magnetization is imaged in situ (**g**) where dark blue indicates spins along $+S^y$. Only the S^x and S^y components of the spin are shown in **c**–**f**.

is strongly affected by nearest-neighbour (off-site) interactions of the underlying Hubbard model which have not been observed before for contact interactions (and therefore all alkali atoms) and can be an important, general effect for quantum simulations with ultracold atoms.

Spin-helix states and the phantom condition. In this work, we study transverse spin-helix states

$$|\psi(Q)\rangle = \prod_i \left[\cos(\theta/2)|\uparrow\rangle_i + \sin(\theta/2)\mathrm{e}^{-\mathrm{i}Qz_i}|\downarrow\rangle_i\right]. \qquad (3)$$

The polar angle θ determines the local longitudinal spin component $\langle S_i^z\rangle = \cos\theta$, which is initially constant along the chain, and z_i is the position of the ith spin (Fig. 1a,b). In the classical limit, any transverse spin helix is stable for any anisotropy since the torques exerted on a given spin by its neighbours cancel exactly[17]. Therefore, the decay of a spin helix is due to quantum fluctuations. However, for wavevectors Q_p fulfilling the phantom condition for $|\Delta|\le 1$ (equation (2)), the fluctuations from the two nearest neighbours also cancel exactly, making these special helices particularly long-lived compared with helix states with any other wavevector. Intriguingly, one can show that they are in fact exact many-body eigenstates of the Heisenberg model (equation (1)) for infinite systems, or for finite systems with appropriate boundary conditions[15]. For the finite chains with open boundaries that we prepared in our experiments, the phantom spin helix is only metastable, as spins at the boundaries have only one neighbour and dephase rapidly. This perturbation propagates into the bulk[17], resulting in a finite decay rate.

For the isotropic system ($\Delta=1$), the phantom spin helix has a wavevector $Q_\mathrm{p}=0$ and thus reduces to a spin-polarized product state for all angles θ (for example, in the S^x direction for $\theta=\pi/2$), which is a trivial eigenstate of this model. For $\Delta=0$, the phantom condition yields $Q_\mathrm{p}a=\pi/2$, so that angles between neighbouring spins are 90° (assuming that all spins lie in the S^x–S^y plane, that is, $\theta=\pi/2$). To explain intuitively how this state is metastable, consider a spin which points, for example, in the S^x direction, with quantum fluctuations in the S^y–S^z plane. Since $J_z=0$, there is no interaction from the S^z component, while the S^y component causes no precession on the neighbouring spins, which also point along the $\pm S^y$ direction. In the following, we demonstrate the existence of these long-lived phantom helices for general Δ and confirm the predictions of the phantom condition (equation (2)).

Experimental methods. As in our previous work[16,17], the spin model is implemented by loading ultracold ^{7}Li atoms in the two lowest hyperfine states into a three-dimensional optical lattice. This system is well described by a two-component Bose–Hubbard model. Two of the three lattice potentials are kept high at $35E_\mathrm{R}$, where $E_\mathrm{R}=h^2/(8ma^2)$ is the recoil energy for atomic mass m with h being the Planck constant, creating a bundle of isolated one-dimensional (1D) chains. The lattice depth of the third axis V_0 is set to a value between $9E_\mathrm{R}$ and $11E_\mathrm{R}$, which is deep enough that the system remains in the Mott insulating regime while still allowing for spin dynamics.

Because particle motion is suppressed in the Mott insulator, the dynamics of the remaining degrees of freedom can be described using a pure spin model. By mapping the two hyperfine states onto spin $|\uparrow\rangle$ and $|\downarrow\rangle$, we can realize the spin-1/2 Heisenberg XXZ model (equation (1)) in which the interactions are mediated by superexchange[19–22]. The longitudinal and transverse spin couplings are given by

$$\begin{aligned} J_z &= +4\tilde{t}^2/U_{\uparrow\downarrow} - 4\tilde{t}^2/U_{\downarrow\downarrow} - 4\tilde{t}^2/U_{\uparrow\uparrow} \\ J_{xy} &= -4\tilde{t}^2/U_{\uparrow\downarrow}, \end{aligned} \qquad (4)$$

where $\tilde{t}$ is the tunnelling matrix element between neighbouring sites and $U_{\uparrow\uparrow}$, $U_{\uparrow\downarrow}$ and $U_{\downarrow\downarrow}$ are the on-site interaction energies. The spin couplings (equation (4)) can be varied over two orders of magnitude by changing the lattice depth V_0, which scales the entire Hamiltonian. We control the anisotropy $\Delta := J_z/J_{xy}$ via an applied magnetic field B, which tunes the interactions through Feshbach resonances[16,17,23]. In our realization, the transverse coupling is antiferromagnetic ($J_{xy}>0$).

The transverse spin helix is created by radiofrequency pulses to tilt the spins to a finite polar angle θ, followed by magnetic field gradients to wind a helix[17,24–26] (Fig. 1c,d and Extended Data Fig. 1). Time evolution is initiated by rapidly lowering V_0. The dynamics following this quench are governed by the 1D XXZ model (equation (1); Fig. 1e) with a selected anisotropy Δ. After a variable evolution time t, the dynamics are frozen by rapidly increasing V_0. The sample is then imaged. Experimental parameters are given in refs. [16,17] and Methods.

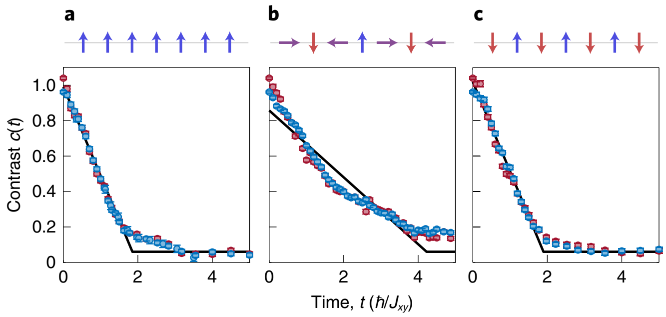

Fig. 2 | Decay of spin-helix states. a–c, The spin-helix contrast $c(t)$ measured for $\Delta \approx 0$ and $\theta = \pi/2$ at two different lattice depths $9E_R$ (red) and $11E_R$ (blue), with corresponding spin-exchange times $\hbar/J_{xy} = 1.06$ and 2.91 ms, for three wavevectors: $Qa = 0$ with all spins aligned (**a**), $Qa = \pi/2$ with neighbouring spins perpendicular (**b**), which is a many-body eigenstate for $\Delta = 0$, and $Qa = \pi$ with all spins anti-aligned (**c**). Their respective spin patterns in the S^x–S^y plane are illustrated by the arrows above each panel. The decay curves at different lattice depths collapse when times are normalized in units of $\hbar/J_{xy}$. The contrast lifetime is significantly longer for $Qa = \pi/2$ compared with $Qa = 0$ or π. The linear fit function captures the decay and averages over an oscillatory beat note between the spin chains and isolated atoms as discussed in ref. [17]. An experimental detection noise floor is on the level of ~0.06. Error bars represent 1σ uncertainty of the fits.

Our imaging system limits the direct observation of spin modulations to a wavelength of $\lambda > 6a$. To image spin helices at any value of Q, we first unwind the remaining spin modulation to a wavelength of $\lambda \approx 10a$ by applying a π-pulse followed by a magnetic field gradient as in Fig. 1f. After unwinding, we turn the transverse helix into a population modulation by applying a π/2 pulse. Finally, we detect the spatial distribution of spin $|\uparrow\rangle$ atoms in situ with state-selective polarization-rotation imaging (Fig. 1g). Compared with our previous work[16,17], this novel unwinding step extends our observable range of wavevectors Q all the way to $Qa = \pi$, where neighbouring spins are anti-aligned. Integrating the images along a direction perpendicular to the chains yields a 1D spatial profile of sinusoidal population modulation over all spin chains (Fig. 1g). The observable is the normalized contrast $c(t)$ of this sinusoidal spin modulation. Due to the lack of exact theory for the decay shape, we fit the whole decay curve by a linear function $(1 - \gamma t)$ to phenomenologically determine a decay rate γ, while accounting for a constant experimental detection noise floor for long times t. (See Methods for details of the fitting.) For the data in Figs. 2 and 3b–d, we measure the spin dynamics at two different lattice depths V_0 and verify that the decay curves $c(t)$ collapse when time is rescaled by the spin-exchange time $\hbar/J_{xy}$, confirming that the spin dynamics is driven by superexchange.

Experimental observations of phantom helices. Figure 2 illustrates the contrast decay $c(t)$ for spin helices with different wavevectors Q at $\Delta \approx 0$. We see that the decay for $Qa = \pi/2$ is noticeably slower than that for $Qa = 0$ or π. This non-monotonic behaviour is the signature of phantom spin helices. This feature is emphasized in Fig. 3 by comparing the contrast decay rates γ as a function of Q for various Δ. Since the superexchange interactions in equation (4) depend on the scattering lengths, we can tune Δ smoothly by varying the magnetic field. In the next section, we confirm that the value of Δ obtained from the observed minimum of the decay rate agrees with the value of Δ derived from equation (4) (with appropriate higher-order corrections) and previously determined scattering lengths[27]. Figure 3 is consistent with a predicted exact symmetry (Methods) in that the decay rate at a wavevector of Q and an anisotropy of Δ is equal to that at a wavevector of $\pi/a - Q$ and an anisotropy of $-\Delta$.

We employ a fit function $\gamma(Q) = \gamma_1|\Delta - \cos(Qa)| + \gamma_0$, derived previously from a short-time expansion of the spin-helix contrast $c(t)$ (ref. [17]). Here, Δ, γ_1 and γ_0 are treated as free fit parameters. γ_1 represents a bulk-intrinsic dephasing decay (for spin helices away from the phantom condition) originating from quantum fluctuations of the spins. Therefore, its magnitude is on the order of the spin coupling $J_{xy}/\hbar$. γ_0 represents a background decay rate accounting for effects such as finite chain length, holes in the spin chains and inhomogeneous lattice depth, which enable dephasing induced by an effective magnetic field $h_z = 4\tilde{t}^2/U_{\uparrow\uparrow} - 4\tilde{t}^2/U_{\downarrow\downarrow}$ (ref. [17]), which is also created by superexchange and, for our experimental situation, is comparable to J_{xy} (Methods and Extended Data Figs. 2 and 3).

We also observe phantom helix states for various polar angles in Fig. 3b–d. This confirms the prediction[15] that there is a whole family of phantom helix states for a given value of Δ. We find that a larger absolute value of the total S^z magnetization (that is, θ close to 0 or π) leads to an overall slower decay. This is expected since such values of θ correspond to states that are almost uniformly polarized along the S^z direction with a small density of quasiparticles (magnons), which gives rise to a small rate of inter-particle scattering events.

For anisotropies $|\Delta| > 1$ (Fig. 3a,e, open symbols) there is no longer a stable spin-helix eigenstate[15]. We see instead that the minimum decay rate always occurs at $Q = 0$ (for $\Delta \geq 1$) and $Qa = \pi$ (for $\Delta \leq -1$). Comparing decay rates across Δ in this range, we find a Q-independent increase relative to the $|\Delta| = 1$ case which is monotonic in $|\Delta| - 1$.

Our improved imaging protocol allows us to access new parameter regimes beyond previous work. For the isotropic system ($\Delta = 1$), we had observed diffusive spin transport characterized by $\gamma(Q) \approx \gamma_1 Q^2 a^2/2 + \gamma_0$ (refs. [16,17,24]). However, we now see this quadratic behaviour break down for large Q when the wavelength λ becomes comparable to the lattice spacing a (Fig. 3a). The fastest decay occurs for the Néel state ($Qa = \pi$), where neighbouring spins are anti-aligned. This directly demonstrates that this classical antiferromagnetic state is not the ground state of the quantum antiferromagnetic Heisenberg Hamiltonian. Nevertheless, the Néel state is an exact highly excited eigenstate for $\Delta = -1$ (Fig. 3e).

Extension to higher dimensions and long-range systems. The phantom spin-helix states were originally discovered in 1D as a coherent superposition of Bethe phantom states, which are special degenerate solutions to the Bethe ansatz equations[15]. This raises the question of whether this phenomenon is tied exclusively to integrability. We find that this is not the case. We can rigorously show that stationary phantom helix states exist for the anisotropic Heisenberg model defined on hypercubic lattices in arbitrary spatial dimensions and for arbitrary spin quantum numbers. A valid phantom spin-helix state in d dimensions is specified by a wavevector $\mathbf{Q} = (Q_1, \cdots, Q_d)$, such that $\mathbf{Q} = \mathbf{Q}_p := Q_p\mathbf{x}$, where $\mathbf{x} \in \{-1, 1\}^d$ is a binary vector of ±1s and Q_p $(0 \leq Q_p a \leq \pi)$ satisfies the phantom condition $\Delta = \cos(Q_p a)$ (equation (2)). The precise statement as well as the corresponding proof is presented in Methods.

Figure 4 demonstrates an example of a two-dimensional spin helix on a two-dimensional (2D) square lattice with a particular winding angle $\phi = Q_p a = 40°$, which is a phantom helix state for the anisotropic Heisenberg model with $\Delta = \cos(40°) \approx 0.771$. Spins along each (horizontal and vertical) line in fact form a one-dimensional phantom helix state with a winding angle of $\phi = Q_p a$. Additionally, note that the 2D model, owing to the nearest-neighbour pairwise nature of its interactions, can be written as a sum of 1D Heisenberg Hamiltonians along each line. One can therefore understand the stability of these 2D phantom helices (as well as higher-dimensional generalizations) as arising from the 1D mechanism of pairwise cancellation of fluctuations demonstrated above.

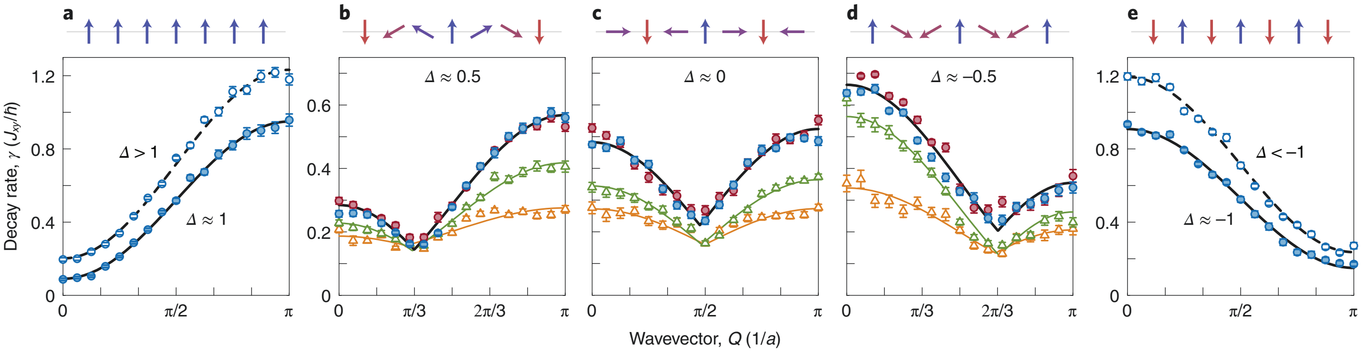

Fig. 3 | Observation of phantom helix states. a–e, The decay rate γ as a function of the wavevector Q, shown for fitted anisotropies Δ ranging from positive (**a**,**b**) through zero (**c**) to negative values (**d**,**e**) measured at lattice depths of $9E_R$ (red) and $11E_R$ (blue). The decay rate minimum occurs at a wavevector Q_p which increases smoothly from $Q_pa = 0$ for $\Delta \approx 1$ (**a**) to $Q_pa = \pi$ for $\Delta \approx -1$ (**e**). Error bars represent 1σ uncertainty of the fits. The long-lived spin pattern in the S^x–S^y plane is illustrated above each panel. Fits $\gamma(Q) = \gamma_1|\Delta - \cos(Qa)| + \gamma_0$ (lines) are used to find Q_p and the anisotropies Δ shown in Fig. 5. In addition to the purely transverse helices (polar angle $\theta = \pi/2$, circles), **b**–**d** also show the decay of spin helices with polar angles $\theta = 5\pi/12$ (green triangles) and $\theta = 2\pi/3$ (orange triangles). The curves above were measured at applied magnetic fields of $B = 847.887$ G ($\Delta > 1$) and 847.286 G ($\Delta \approx 1$) (**a**), 845.760 G (**b**), 842.905 G (**c**), 839.376 G (**d**), 833.004 G ($\Delta \approx -1$) and 827.287 G ($\Delta < -1$) (**e**). The shape of the decay rates $\gamma(Q)$ for $\Delta > 1$ ($\Delta < 1$) is identical to those for $\Delta = 1$ ($\Delta = -1$). Both are pure cosines with an offset. In the absence of a full theory for the amplitude of oscillation γ_1 and the offset γ_0, we cannot determine the value of Δ for $|\Delta| > 1$.

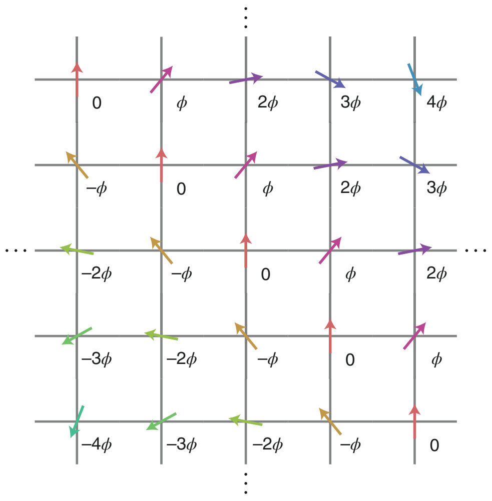

Fig. 4 | A 2D phantom spin helix for the anisotropic Heisenberg model with $\Delta = \cos(40^\circ) \approx 0.771$. The spin helix has a wavevector $\mathbf{Q} = (Q_x, Q_y) = (Q_p, Q_p)$, with $\phi = Q_pa = 40°$. The azimuthal angle of the spin in the transverse plane is labelled for each vertex. Spins with the same angle are encoded with the same colour to guide the eye.

Non-trivial phantom helix states also exist for non-hypercubic lattices, for example, triangular and kagome lattices, provided that the winding angle and anisotropy are 'compatible' with the geometry of the lattice (Extended Data Fig. 4). Specifically, this requires anisotropy $\Delta = -1/2$, giving rise to $\phi = \pm 2\pi/3$ (Methods and refs. [28,29]).

Our experimental protocol can be extended to phantom states in higher dimensions to observe the associated quantum scarred dynamics. After initializing a spin-polarized sample at high fields near a Feshbach resonance, we would ramp to a low field where we can wind spin helices in arbitrary directions, not limited by the direction of the high bias field. Subsequently, we would return to high Feshbach fields where we can simulate the XXZ model, and finally return to a low field to unwind and measure the contrast for different evolution times. The full procedure and current technical limitations are described in Methods.

Lastly, we mention that there exist certain long-range deformations to the spin-1/2 model in 1D which break integrability yet retain the phantom helix as an exact eigenstate (Methods and Extended Data Fig. 5).

Measurement of anisotropy. Besides being of fundamental interest, the phantom helix states also have applications in quantum simulations. We can use the sensitivity of the phantom helix states to measure the spin-exchange anisotropy $\Delta = J_z/J_{xy}$ precisely as a function of the applied magnetic field B (Fig. 5). Until now, there has been no protocol to directly measure Δ. It could only be estimated[16,17] from measured scattering lengths $a_{\uparrow\uparrow}$, $a_{\uparrow\downarrow}$ and $a_{\downarrow\downarrow}$ (refs. [23,27]) using equation (4). Figure 5 compares our measured Δ with the predictions based on scattering lengths. They agree quite well away from Feshbach resonances, where we expect equation (4) to be accurate with some well-established corrections (Methods and Fig. 5). This validates the method of using the phantom phenomenon to determine Δ even in situations where a microscopic theory is not available or not accurate, for example, when there are strong interactions near Feshbach resonances (Methods).

We first discuss the accuracy of our determination of Δ and possible systematic errors. Repeated measurements of Δ are reproducible to better than 0.1, as is clearly visible by the small random scatter of the data points in Fig. 5. In addition, there are possible systematic effects. For one, the observed decay is non-exponential and our fit function $\gamma(Q) = \gamma_1|\Delta - \cos(Qa)| + \gamma_0$ was derived from a short-time quadratic expansion of the decay of contrast[17]. Experimentally, however, we can only observe the contrast at intermediate times where the decay is more linear (as already discussed in previous work[16,17,24]). The most robust and consistent fits were obtained with a linear function $(1 - \gamma t)$, where γ is the decay rate. Additionally, some of the contrast decay curves have an oscillatory component which averages out for long but not shorter decay times. By using different fit functions (exponential, linear, with or without oscillating terms and different constraints for the fit parameters) for our data and numerically simulated data, we find that $|\Delta|$ in Fig. 5 could be overestimated. At $|\Delta| \approx 0.5$, the overestimation is the most severe and can be up to 0.15 (30%), but it is smaller (≈0.05) for $|\Delta|$ closer to 0 and 1.

Furthermore, a systematic shift of $|\Delta|$ could also occur if there were a Q-dependent background decay mechanism, although preliminary investigations provide no evidence that such an effect

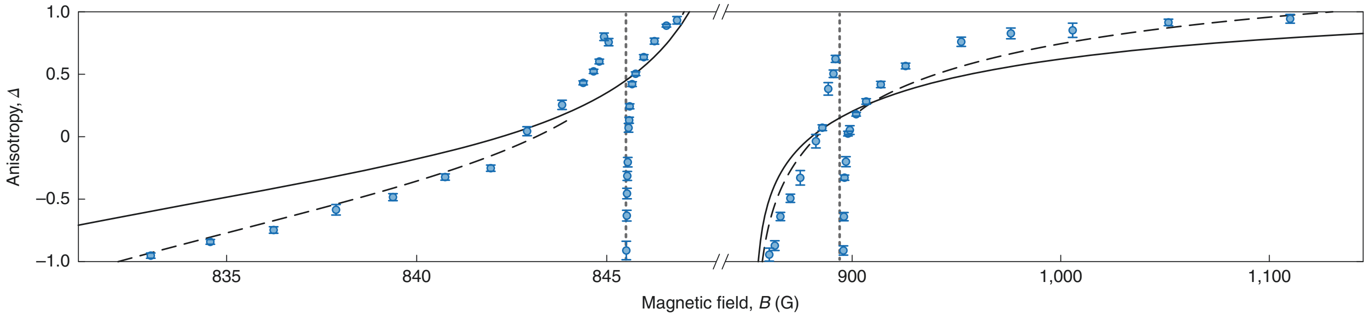

Fig. 5 | Tuning the anisotropy with magnetic fields. Measured anisotropies Δ (blue circles) compared with the standard model for superexchange given by equation (4) (solid line) using previously measured scattering lengths[27]. Error bars represent 1σ uncertainty of the fits. The dashed black line includes next-order corrections to the underlying Hubbard model including bond-charge tunnelling, higher-order band corrections and off-site interactions[30], as well as a small adjustment of the background scattering length of $a_{\uparrow\downarrow}$, which was not tightly constrained by previous measurements. The dashed lines are not shown near Feshbach resonances because equation (4), even with corrections, is no longer valid. Major deviations near the two ↑↑ Feshbach resonances at 845.506 and 893.984 G (vertical dotted lines) are evidence for off-site interactions.

exists (Methods). Several of these issues could be addressed experimentally in the future by using a quantum gas microscope and observing the dynamics in single isolated spin chains.

The 'dispersive' shape of Δ near the two Feshbach resonances in Fig. 5 cannot be explained by the 'standard' superexchange model of equation (4), since these spin coupling parameters depend on $1/U_{\uparrow\uparrow}$ and therefore vary smoothly across the resonance. The leading-order corrections to the underlying standard Hubbard model[16,30,31] include bond-charge tunnelling[32], higher-band corrections to U (refs. [33,34]) and off-site contact interactions V (ref. [16]). As long as the extended Hubbard model involves only nearest-neighbour terms, the spin physics of a Mott insulator phase at unity filling is still described by the anisotropic Heisenberg model of equation (1) (Methods).

Of the various corrections to the standard Hubbard model[30], only contributions from off-site interactions have the correct symmetry and sign to explain the observed dispersive feature (Methods). Therefore, the phantom helix states reveal that spin–spin interactions near a Feshbach resonance are caused by off-site interactions which have never been observed for contact interactions (they have only been observed for long-range dipolar interactions[35]) or a new form of interactions. Off-site interactions originate from the small overlap of a Wannier function on one site with those of its nearest neighbours[36] and add a correction term to J_z in equation (4) of $2(V_{\uparrow\uparrow}+V_{\downarrow\downarrow}-2V_{\uparrow\downarrow})$ (ref. [16]), where $V_{\uparrow\uparrow}$, $V_{\uparrow\downarrow}$ and $V_{\downarrow\downarrow}$ are the off-site interaction energies. However, as we will explore in future work, the current model for off-site interactions[30,31,36] cannot fully explain our observations, and a more elaborate theory is needed to account for the correct spin Hamiltonian near a Feshbach resonance.

Discussion and outlook. Previous studies of the Heisenberg model have focused on the ground state[37–39], low-lying elementary excitations including magnons[40,41] and Bethe strings[42,43], or on unstable dynamics far from equilibrium[14,16,17,24,44]. This work captures a new class of excitations: phantom spin-helix states. These are highly excited yet long-lived metastable states whose stability is not the result of symmetry but rather due to a delicate cancellation of interactions. In fact, such atypical, slow dynamics are not only specific to the Heisenberg model but also expected to be exhibited by other integrable systems, as expounded in ref. [15]. Our experimental findings thus constitute a concrete demonstration of this novel, general dynamical phenomenon.

More broadly, we have theoretically explored spin-helix states in systems with higher spatial dimensions, for different spin quantum numbers, in various lattice geometries and with longer-range interactions, all of which are not integrable. Nevertheless, we find that, for the special initial condition of a phantom helix state, the system does not relax at all, despite the presence of strong interactions. Such non-thermalizing dynamics in non-integrable, many-body systems constitute examples of 'weak ergodicity-breaking', or what are now known as 'quantum many-body scars'[18]. While various toy models hosting exact quantum many-body scars have already been discussed in literature, such models are primarily theoretical constructs which are difficult to realize experimentally[45–48]. In contrast, we demonstrate that one of the simplest examples of a many-body system (the XXZ Heisenberg model) can support quantum many-body scars, a fact which has been overlooked thus far. The relative simplicity implies that probing such scarred dynamics experimentally is relatively straightforward, and in Methods we propose how our current protocol can be extended to higher dimensions.

We expect phantom helix states to have applications in quantum simulations of spin physics. We have demonstrated the potential of the phantom helix states as a sensitive tool to directly measure the anisotropy Δ. They have revealed that even short-range interactions can lead to strong off-site interactions in spin models. This can now be used to realize extended Hubbard models[31,36] including the quantum lattice gas (or t–V) model[49] which supports a supersolid phase[50]. In the future, these long-lived helix states could be an intermediate step in preparing other many-body quantum states or be used for robust quantum sensing[51]. It has been shown that phantom helix states maintain the classical topological protection of winding patterns[52]. An intriguing question is what will ultimately limit the stability of these states if periodic boundary conditions are realized with ring-shaped atom arrays[53]. Such studies are likely to provide new insight into spin dynamics far from equilibrium.

Online content

Any methods, additional references, Nature Research reporting summaries, source data, extended data, supplementary information, acknowledgements, peer review information; details of author contributions and competing interests; and statements of data and code availability are available at https://doi.org/10.1038/s41567-022-01651-7.

Received: 24 January 2022; Accepted: 23 May 2022;

References

1. Berges, J. et al. Prethermalization. *Phys. Rev. Lett.* **93**, 142002 (2004).
2. Rigol, M. et al. Relaxation in a completely integrable many-body quantum system: an ab initio study of the dynamics of the highly excited states of 1D lattice hard-core bosons. *Phys. Rev. Lett.* **98**, 050405 (2007).

3. Gring, M. et al. Relaxation and prethermalization in an isolated quantum system. *Science* **337**, 1318–1322 (2012).
4. Eigen, C. et al. Universal prethermal dynamics of Bose gases quenched to unitarity. *Nature* **563**, 221–224 (2018).
5. Abanin, D. A. et al. Many-body localization, thermalization, and entanglement. *Rev. Mod. Phys.* **91**, 021001 (2019).
6. Choi, S. et al. Observation of discrete time-crystalline order in a disordered dipolar many-body system. *Nature* **543**, 221–225 (2017).
7. Zhang, J. et al. Observation of a discrete time crystal. *Nature* **543**, 217–220 (2017).
8. Arute, F. et al. Quantum supremacy using a programmable superconducting processor. *Nature* **574**, 505–510 (2019).
9. Flamini, F. et al. Photonic quantum information processing: a review. *Rep. Prog. Phys.* **82**, 016001 (2018).
10. Kinoshita, T. et al. A quantum Newton's cradle. *Nature* **440**, 900–903 (2006).
11. Žnidarič, M. Spin transport in a one-dimensional anisotropic Heisenberg model. *Phys. Rev. Lett.* **106**, 220601 (2011).
12. Ljubotina, M. et al. Spin diffusion from an inhomogeneous quench in an integrable system. *Nat. Commun.* **8**, 16117 (2017).
13. Ljubotina, M. et al. Kardar–Parisi–Zhang physics in the quantum Heisenberg magnet. *Phys. Rev. Lett.* **122**, 210602 (2019).
14. Wei, D. et al. Quantum gas microscopy of Kardar-Parisi-Zhang superdiffusion. *Science* **376**, 716–720 (2022).
15. Popkov, V. et al. Phantom Bethe excitations and spin helix eigenstates in integrable periodic and open spin chains. *Phys. Rev. B* **104**, L081410 (2021).
16. Jepsen, P. N. et al. Spin transport in a tunable Heisenberg model realized with ultracold atoms. *Nature* **588**, 403–407 (2020).
17. Jepsen, P. N. et al. Transverse spin dynamics in the anisotropic Heisenberg model realized with ultracold atoms. *Phys. Rev. X* **11**, 041054 (2021).
18. Serbyn, M. et al. Quantum many-body scars and weak breaking of ergodicity. *Nat. Phys.* **17**, 675–685 (2021).
19. Kuklov, A. B. et al. Counterflow superfluidity of two-species ultracold atoms in a commensurate optical lattice. *Phys. Rev. Lett.* **90**, 100401 (2003).
20. Duan, L. M., Demler, E. & Lukin, M. D. Controlling spin exchange interactions of ultracold atoms in optical lattices. *Phys. Rev. Lett.* **91**, 090402 (2003).
21. García-Ripoll, J. J. & Cirac, J. I. Spin dynamics for bosons in an optical lattice. *N. J. Phys.* **5**, 76–76 (2003).
22. Altman, E. et al. Phase diagram of two-component bosons on an optical lattice. *N. J. Phys.* **5**, 113 (2003).
23. Amato-Grill, J. et al. Interaction spectroscopy of a two-component Mott insulator. *Phys. Rev. A* **99**, 033612 (2019).
24. Hild, S. et al. Far-from-equilibrium spin transport in Heisenberg quantum magnets. *Phys. Rev. Lett.* **113**, 147205 (2014).
25. Koschorreck, M. et al. Universal spin dynamics in two-dimensional Fermi gases. *Nat. Phys.* **9**, 405–409 (2013).
26. Trotzky, S. et al. Observation of the Leggett–Rice effect in a unitary Fermi gas. *Phys. Rev. Lett.* **114**, 015301 (2015).
27. Secker, T. et al. High-precision analysis of Feshbach resonances in a Mott insulator. *Phys. Rev. A* **101**, 042703 (2020).
28. Changlani, H. J. et al. Macroscopically degenerate exactly solvable point in the spin-1/2 kagome quantum antiferromagnet. *Phys. Rev. Lett.* **120**, 117202 (2018).
29. Lee, K. et al. Exact three-colored quantum scars from geometric frustration. *Phys. Rev. B* **101**, 241111 (2020).
30. Lühmann, D. S. Multi-orbital and density-induced tunneling of bosons in optical lattices. *N. J. Phys.* **14**, 033021 (2012).
31. Dutta, O. et al. Non-standard Hubbard models in optical lattices: a review. *Rep. Prog. Phys.* **82**, 016001 (2018).
32. Jürgensen, O. et al. Observation of density-induced tunneling. *Phys. Rev. Lett.* **113**, 193003 (2014).
33. Campbell, G. K. et al. Imaging the Mott insulator shells by using atomic clock shifts. *Science* **313**, 649–652 (2006).
34. Will, S. et al. Time-resolved observation of coherent multi-body interactions in quantum phase revivals. *Nature* **465**, 197–201 (2010).
35. Baier, S. et al. Extended Bose–Hubbard models with ultracold magnetic atoms. *Science* **352**, 201–205 (2016).
36. Amadon, J. C. et al. Metallic ferromagnetism in a single-band model: effect of band filling and Coulomb interactions. *Phys. Rev. B* **54**, 6364 (1996).
37. Parsons, M. F. et al. Site-resolved measurement of the spin-correlation function in the Fermi–Hubbard model. *Science* **353**, 1253–1256 (2016).
38. Cheuk, L. W. et al. Observation of spatial charge and spin correlations in the 2D Fermi–Hubbard model. *Science* **353**, 1260–1264 (2016).
39. Mazurenko, A. et al. A cold-atom Fermi–Hubbard antiferromagnet. *Nature* **545**, 462–466 (2017).
40. Fukuhara, T. et al. Quantum dynamics of a mobile spin impurity. *Nat. Phys.* **9**, 235–241 (2013).
41. Fukuhara, T. et al. Microscopic observation of magnon bound states and their dynamics. *Nature* **502**, 76–79 (2013).
42. Wang, Z. et al. Experimental observation of Bethe strings. *Nature* **554**, 219–223 (2018).
43. Bera, A. K. et al. Dispersions of many-body Bethe strings. *Nat. Phys.* **16**, 625–630 (2020).
44. Nichols, M. A. et al. Observation of spatial charge and spin correlations in the 2D Fermi–Hubbard model. *Science* **363**, 383–387 (2019).
45. Shiraishi, N. et al. Systematic construction of counterexamples to the eigenstate thermalization hypothesis. *Phys. Rev. Lett.* **119**, 030601 (2017).
46. Mark, D. K. et al. Unified structure for exact towers of scar states in the Affleck–Kennedy–Lieb–Tasaki and other models. *Phys. Rev. B* **101**, 195131 (2020).
47. Chattopadhyay, S. et al. Quantum many-body scars from virtual entangled pairs. *Phys. Rev. B* **101**, 174308 (2020).
48. Moudgalya, S. et al. η-Pairing in Hubbard models: from spectrum generating algebras to quantum many-body scars. *Phys. Rev. B* **102**, 085140 (2020).
49. Cazalilla, M. A. et al. One dimensional bosons: from condensed matter systems to ultracold gases. *Rev. Mod. Phys.* **83**, 1405–1466 (2011).
50. Matsuda, H. et al. Off-diagonal long-range order in solids. *Prog. Theor. Phys. Suppl.* **46**, 411–436 (1970).
51. Dooley, S. Robust quantum sensing in strongly interacting systems with many-body scars. *PRX Quantum* **2**, 020330 (2021).
52. Posske, T. Winding up quantum spin helices: how avoided level crossings exile classical topological protection. *Phys. Rev. Lett.* **122**, 097204 (2019).
53. Scholl, P. et al. Microwave-engineering of programmable XXZ Hamiltonians in arrays of Rydberg atoms. PRX Quantum **3**, 020303 (2022).

Methods

Experimental methods. As described in previous work[16], we prepare 4.5×10^{47} Li atoms in an optical lattice with spacing $a=532$ nm in the Mott insulating regime with one atom per site in the $|\uparrow\rangle$ state. The lowest and second-lowest hyperfine states of ^{7}Li realize the $|\downarrow\rangle$ and $|\uparrow\rangle$ state, respectively. The Mott insulator diameter is approximately 44 lattice sites, of which doublons account for less than 0.5% while holes are estimated to represent 5–10%. The density degree of freedom is frozen out after loading into the deep optical lattice ($35E_R$, where $E_R/h=25.12$ kHz), and the on-site interactions $U_{\uparrow\uparrow}$, $U_{\uparrow\downarrow}$ and $U_{\downarrow\downarrow}$ can be varied freely by using an externally applied magnetic field B to adjust the anisotropy Δ without affecting the global atom distribution, as long as the atoms stay in the Mott insulating regime[54]. We profiled the Feshbach resonance extensively in our previous work[27]. The finite size of the lattice beams introduces small inhomogeneities of the lattice depths, which has been described in detail in ref. [16].

In a deep lattice, a global radiofrequency pulse is used to rotate all the spins by an angle θ away from the initial $|\uparrow\rangle$ state

$$|\psi\rangle=\prod_i[\cos(\theta/2)|\uparrow\rangle_i+\sin(\theta/2)|\downarrow\rangle_i]. \tag{5}$$

Most of our experiments are on purely transverse spin patterns where $\theta=\pi/2$, generating an S^x polarized state $|\psi\rangle=\prod_i[|\uparrow\rangle_i+|\downarrow\rangle_i]/\sqrt{2}$. An applied magnetic field gradient in the z direction causes spin precession at rates which depend linearly on the position z_i of the spin, thus creating a spin helix[17,24–26]

$$|\psi\rangle=\prod_i[\cos(\theta/2)|\uparrow\rangle_i+\mathrm{e}^{-\mathrm{i}Qz_i}\sin(\theta/2)|\downarrow\rangle_i]. \tag{6}$$

We apply a magnetic field gradient of up to 39 G cm^{-1} over a time of up to 8 ms to wind the spin helix. We calibrate the spin winding process against the duration and magnitude of the applied gradient by overwinding the spin helix beyond $Qa\approx2\pi$. Since the wavevectors Q and $Q+2\pi/a$ correspond to the same state, we obtain an absolute calibration of winding angle versus time-integrated gradient. In other words, our wavevectors Q are measured directly in units of the lattice spacing a, independent of the (less accurately known) imaging magnification. All helices with directly observable Q fall on a line in Extended Data Fig. 1. This allows us to find the winding time and gradient required for helices with wavevectors Q which we cannot image directly.

After winding the spin helix, we initiate spin dynamics in 1D chains by ramping down the lattice depth along one direction to $9E_R$ or $11E_R$, which is small to enable fast superexchange but still large enough to stay in the Mott insulating regime. The ramp time is 0.5 ms, fast compared to the superexchange time $\hbar/J_{xy}$ (ranging from 1 to 4 ms) but slower than the inverse of the interaction energies $\hbar/U_{\uparrow\uparrow}$, $\hbar/U_{\uparrow\downarrow}$ and $\hbar/U_{\downarrow\downarrow}$ (<0.05 ms), thus realizing a quantum quench for the spin sector of the Mott insulator. At a lattice depth of $11E_R$, the tunnelling rate is $\tilde{t}/h\approx380$ Hz and the on-site interactions $U_{\downarrow\downarrow}$ and $U_{\uparrow\downarrow}$ vary weakly as a function of the external magnetic field (ranging from $U_{\downarrow\downarrow}/h=-6.8$ to -3.0 kHz and from $U_{\uparrow\downarrow}/h=-11.0$ to -2.9 kHz in the magnetic field range of $B=830$ to 1,150 G used in our experiments), whereas $U_{\uparrow\uparrow}$ can be tuned via Feshbach resonances to arbitrary positive and negative values. After a variable evolution time t, the spin dynamics is frozen by increasing the lattice depth back to $35E_R$ (where the tunnelling rate is $\tilde{t}/h=5$ Hz) within 0.5 ms, followed by an unwinding step to a resolvable readout wavevector $Q\approx2\pi\times0.1/a$, which allows us to measure the contrast of high-Q spin helices indirectly.

As described in refs. [16,17], we determine the contrast C by a fit $f(z)=g(z)[1+C\cos(Qz)]/2$, where $g(z)$ is a Gaussian envelope function that accounts for the spatial distribution of all atoms. During the evolution time t, the contrast $C(t)$ decays. We fit the decay rate of the normalized contrast $c(t):=C(t)/C(0)$. The decay rate at early times should be quadratic (see discussion below and ref. [17]), but because we cannot observe the system at $t=0$ and the exact decay shape is not known, we use a linear fit to phenomenologically determine a decay rate. For long evolution times t the contrast $c(t)$ approaches an experimental detection noise floor on the level of ~0.06.

Discussion of decay rates. In the main text, we found that the measured decay rates of spin helices obeyed well the fit function

$$\gamma(Q)=\gamma_1|\Delta-\cos(Qa)|+\gamma_0. \tag{7}$$

Here, we discuss the physical interpretation of the terms associated with γ_1 and γ_0. We also discuss which experimental techniques can eliminate the mechanisms that contribute to γ_0 which would lead to very long lifetime of the phantom helix state. In our experiment, the bulk-intrinsic dephasing rate γ_1 and the background decay γ_0 are comparable. Nevertheless, γ_0 is small enough that the signature $\gamma_1|\Delta-\cos(Qa)|$ of the phantom helix states can clearly be observed and distinguished from the background decay γ_0.

Bulk decay rate γ_1. As mentioned above, the contribution $\gamma_1|\Delta-\cos(Qa)|$ was derived via a short-time expansion of the contrast $c(t)$ for general spin helices evolving under the 1D Heisenberg model[17]. Therefore, this term can be understood as arising from the intrinsic decay associated with a spin helix with wavevector not equalling the phantom wavevector $Q\neq Q_p$. The rate γ_1 scales as J_{xy} but is also set by the effective exchange coupling of spins, determined by the quasiparticle (magnon) density in the system, which can be tuned by the polar angle θ. In particular, at low densities (which translates to $\theta\approx0$ or π), γ_1 is small. Indeed, for $\theta=0$ (π), the spin helix for any Q is a spin-polarized state in the $+S^z$ ($-S^z$) direction, which is trivially an eigenstate for any anisotropy Δ. Hence $\gamma_1=0$ for these angles. That is, such a 'spin helix' does not decay.

Boundary conditions. The derivation of this decay mechanism assumed an infinitely long chain. For finite chains, precise boundary conditions matter. The phantom helix state is only an eigenstate if the system has periodic boundary conditions and its wavevector is commensurate with the system size, or if the system has open boundary conditions with appropriate pinning fields at the ends of the chains[15]. Therefore, for generic finite, open chains, even a phantom helix (that is, with Q satisfying $\Delta=\cos(Qa)$) will decay as spins at the boundaries will start to precess and disturb neighbouring spins, and such perturbations propagate into the bulk and destroy the spin-helix pattern[17]. This contribution to γ_0 should scale as $\sim J_{xy}/L$ and can be suppressed by long chains or using ring-shaped geometries[53] realizing periodic boundary conditions.

Effective magnetic field. The situation of finite, open chains is realized in our experimental platform. Important contributions to γ_0 originate from an effective magnetic field $h_z=4\tilde{t}^2/U_{\uparrow\uparrow}-4\tilde{t}^2/U_{\downarrow\downarrow}$ as described in our previous work[17]. This effective field has only half its value at the ends of the chain and therefore modifies the boundary condition by acting as a pinning field.

The effective magnetic field can lead to another contribution to γ_0 if it is inhomogeneous across the cloud. This causes inhomogeneous broadening across different chains and a beat note between the chains and isolated atoms[17]. Such effects can be eliminated by using spin-echo techniques (see previous work[17] detailing this), or by experiments where individual chains are resolved by using imaging with single-site resolution. The effective magnetic field is absent for hyperfine states with $U_{\uparrow\uparrow}=U_{\downarrow\downarrow}$, often fulfilled in experiments with rubidium atoms.

Holes. An additional contribution can come from the presence of holes (with an estimated fraction of 5–10%) in the Mott insulator. Holes near the ends of the chain are localized by the trapping potential[54], effectively shortening the chains (Extended Data Fig. 2)[17]. Mobile holes give rise to a number of effects. First, they create effectively fluctuating spin couplings and local magnetic fields. This leads to a dephasing of transverse spin, leading to a loss of contrast. Second, when holes move around, they can create 'phase slips' in the spin-helix pattern, mismatches in the winding angles between adjacent spins, such that interaction from two neighbouring spins do not cancel but instead cause dephasing. The effects of mobile holes can be reduced by pinning them to their original locations using a sufficiently strong potential gradient, as we showed in previous work[54].

Q dependence of γ_0. If the background decay rate γ_0 has a Q dependence, it can shift the minimum of the decay rate from the phantom condition $\Delta=\cos(Q_pa)$ and hence lead to a systematic error in the measurement of Δ. We investigate the edge effect by numerically simulating spin dynamics on open chains, and extract the total decay rate $\gamma(Q)$ through an early-time fit (Extended Data Fig. 3). We see that there is no shift in the decay minimum, even though there is now a finite decay rate at the phantom condition. For the experimental data, we must extend fitting to longer times. Applying this to simulated decay curves, which have a non-exponential shape, can lead to differences in $|\Delta|$ of up to 0.15 when the contrast decay $c(t)$ is fitted with different functions.

Note that, when random phase shifts are applied to each spin, the contrast reduction does not depend on Q. This is a simplified model for the fluctuating effective magnetic field due to mobile holes[17]. Our understanding of the Q dependence or Q independence of decay rates is incomplete, but it is consistent with the experimental observation that γ_0 appears to be independent of Q (owing to the goodness of the fit of equation (7) to the experimental data). This gives us confidence in the ability to determine Δ reliably from the phantom condition.

Decay rates for 2D spin helices. We expect the bulk decay rate γ_1 to exhibit similar behaviour and magnitude as in 1D. For the background decay rate γ_0, the contribution from boundary effects should also be comparable. Although the boundary of a 2D system is 1D in nature (and thus scales with the linear dimension L of the system), the 'signal' ($\sim L^2$) to 'noise' ($\sim L$) ratio scales in the same fashion as in 1D (L:1). The effect of mobile holes can potentially be more severe in 2D because phase slips can proliferate. A hole that has moved l sites typically leaves $\mathcal{O}(l)$ phase slips in its wake. In contrast, in 1D, such phase slips are localized (but mobile) objects. Mobile holes can be pinned by a potential gradient (see above).

Decay rates for polar angles $\theta\neq\pi/2$. We discussed above that a transverse spin helix with finite S^z magnetization should exhibit a reduced decay rate γ_1. This should also apply to the background decay rate γ_0 associated with the edges of the chain. This expectation is consistent with our observation in Fig. 3c,d. However, the observed effect is comparable to long-term experimental drifts in γ_0 due to changes in atom number and hole fraction.

Symmetry in decay rates. We elaborate on our comment made in the main text that the decay rate at wavevector Q and anisotropy Δ is equal to that at $\pi - Q$ and anisotropy $-\Delta$. Here we set the lattice spacing to $a = 1$ for brevity.

This symmetry in fact stems from a symmetry of the contrast $c(t)$ between parameters (Q,Δ) and $(\pi - Q, -\Delta)$. To see this, consider the extraction of the contrast at (Q,Δ). This first involves a measurement of the local magnetization in the transverse plane, which without loss of generality we take to be in the S^x direction:

$$\langle S_n^x(t)\rangle_{Q,\Delta} = \langle\psi(Q)|\, \mathrm{e}^{\mathrm{i}H(\Delta)t} S_n^x \mathrm{e}^{-\mathrm{i}H(\Delta)t}\, |\psi(Q)\rangle\,. \tag{8}$$

In the above, $H(\Delta)$ is the Heisenberg model with anisotropy Δ and $|\psi(Q)\rangle$ is the spin-helix state with wavevector Q. We can insert identity operators $1 = U^\dagger U = UU^\dagger$ in between the states, time-evolution operators and observable, in the above expression, where U is the unitary transformation $U = \prod_n \mathrm{e}^{\mathrm{i}\pi n S_n^z}$. Now, under U, we have the following transformations: $|\psi(Q)\rangle \mapsto |\psi(Q-\pi)\rangle$, $H(\Delta) \mapsto -H(-\Delta)$ and $S_n^x \mapsto (-1)^n S_n^x$. We can further take a complex conjugation over the entire quantity, which is invariant due to it being real-valued (as it constitutes a measurement), however now its individual constituents change as follows: $|\psi(Q-\pi)\rangle \mapsto |\psi(\pi - Q)\rangle$, $i \mapsto -i$, $-H(-\Delta) \mapsto -H(-\Delta)$ and $S_n^x \mapsto S_n^x$. Therefore, we have

$$\langle S_n^x(t)\rangle_{Q,\Delta} = (-1)^n \langle S_n^x(t)\rangle_{\pi - Q, -\Delta}. \tag{9}$$

Next, the contrast is determined from the Fourier component at wavevector Q:

$$c(t)_{Q,\Delta} = \frac{2}{L}\sum_n \langle S_n^x(t)\rangle_{Q,\Delta} \cos(Qn + \phi), \tag{10}$$

where ϕ is the initial phase of the helix. Using equation (9) and the trigonometric identity $(-1)^n \cos(Qn+\phi) = \cos((\pi - Q)n - \phi)$ for $n \in \mathbb{Z}$, we have

$$\begin{aligned} c(t)_{Q,\Delta} &= \tfrac{2}{L}\sum_n \langle S_n^x(t)\rangle_{\pi-Q,-\Delta}(-1)^n \cos(Qn+\phi) \\ &= \tfrac{2}{L}\sum_n \langle S_n^x(t)\rangle_{\pi-Q,-\Delta} \cos((\pi - Q)n - \phi) \\ &= c(t)_{\pi-Q,-\Delta}, \end{aligned} \tag{11}$$

as claimed.

Higher dimensions, arbitrary spin quantum numbers and non-hypercubic geometries. In this section, we extend the phenomenology of stable phantom helices to Heisenberg models in higher dimensions, arbitrary spin quantum numbers and non-hypercubic geometries. Specifically, we prove that, for any given anisotropy in the easy plane $|\Delta| \le 1$, there exist phantom helices which are exact many-body eigenstates of the model, provided the phantom condition (equation (2)) holds and appropriate boundary conditions are taken.

Model and spin-helix states. We consider the quantum Heisenberg XXZ model for any spatial dimensionality d, spin S and lattice geometry. The Hamiltonian is given by a sum over pairwise nearest-neighbour interactions (we set $J_{xy} = 1$ for simplicity):

$$H(\Delta) := \sum_{\langle ij\rangle} (S_i^x S_j^x + S_i^y S_j^y) + \Delta S_i^z S_j^z, \tag{12}$$

where S_i^α $(\alpha = x, y, z)$ are spin-S operators.

The generalization of a spin-helix state from the spin-1/2 case (equation (3)) is given by

$$|\psi(\mathbf{Q})\rangle = \prod_i \left[\mathrm{e}^{-\mathrm{i}\mathbf{Q}\cdot\mathbf{r}_i S_i^z} \mathrm{e}^{-\mathrm{i}\theta S_i^y} |S\rangle_i\right]. \tag{13}$$

Here, $|S\rangle_i$ is the local maximal spin state satisfying $(\mathbf{S}_i \cdot \mathbf{S}_i)|S\rangle_i = S(S+1)|S\rangle_i$ and $S_i^z|S\rangle_i = S|S\rangle_i$. $\mathbf{Q} = (Q_1, \cdots, Q_d)$ is a d-dimensional wavevector parameterizing the winding rate and direction of the helix, and $\mathbf{r}_i$ is the coordinate of the spin at site i. Therefore, equation (13) locally describes a state created by rotation by angle θ from the z-polarized state around the S^y axis, before a winding in the S^x–S^y plane by a site-dependent angle $\mathbf{Q}\cdot\mathbf{r}_i$.

Statement of results. For the model and state above, we have the following statements (where we set the lattice spacing to $a = 1$ for brevity):

Theorem 1. **(phantom spin helices for the hypercubic lattice)**. Consider a d-dimensional hypercubic lattice of volume $L_1 \times L_2 \times \ldots \times L_d$ and the anisotropic spin-S Heisenberg model with anisotropy Δ defined on it. Let $|\Delta| \le 1$, which we parameterize as $\Delta = \cos(Q_\mathrm{p})$ (the 'phantom condition') for $Q_\mathrm{p} \in [0, \pi)$. Define the wavevector $\mathbf{Q}_\mathrm{p} := Q_\mathrm{p}\mathbf{x}$ where $\mathbf{x}$ is a binary vector $\mathbf{x} = (x_1, \cdots, x_d) \in \{-1, 1\}^d$, and suppose that the linear dimensions L_i are such that $L_i = 2\pi_i/Q_\mathrm{p}$ for some $m_i \in \mathbb{N}$. Then, the spin helix with wavevector $\mathbf{Q}_\mathrm{p}$ and any polar angle θ is an exact eigenstate of the model with energy $E = S^2\cos(Q_\mathrm{p}) \times \#\mathrm{Links}$.

Theorem 2. **(phantom spin helices for the 2D triangular and kagome lattices)**. Consider a 2D regular triangular or kagome lattice and the anisotropic spin-S Heisenberg model with anisotropy $\Delta = -1/2$ defined on it. Define $Q_\mathrm{p} = 2\pi/3$ so that $\cos(2\pi/3) = -1/2 = \Delta$. Then the spin helix with wavevector $\mathbf{Q}_p = (2Q_p, 0)$ or $(4Q_p, 0)$ and any polar angle θ, is an exact eigenstate of the model with energy $E = S^2\cos(Q_p) \times \#\mathrm{Links}$, provided the lattice dimensions are such that it is commensurate with the helix pattern.

Remarks. Figure 4 shows an illustration of the phantom helix for a 2D square lattice, while Extended Data Fig. 4 shows the phantom helix for the 2D triangular and kagome lattices. Note that the phantom helix state for the triangular lattice is known as the 120° Néel ordered state in condensed matter physics, which is the ground state of the classical antiferromagnetic Heisenberg model. For the kagome lattice, it is also known as the $\sqrt{3} \times \sqrt{3}$ state (Extended Data Fig. 4). We show here that they are exact eigenstates for the quantum Heisenberg model at $\Delta = -1/2$. Note that the phantom helix states that we discuss here for triangular and kagome lattices are in fact special cases of more general, so-called three-colour states, discussed in refs. [28,29], which can be shown to be exact ground states of the spin-1/2 model at $\Delta = -1/2$. Our result recovers this result and extends it by showing that the phantom spin helices are also exact eigenstates of the model for all spin quantum numbers.

Proof. Define the local term of the Hamiltonian

$$h_{ij} = (S_i^x S_j^x + S_i^y S_j^y) + \cos(Q_\mathrm{p}) S_i^z S_j^z \tag{14}$$

so that $H(\cos(Q_\mathrm{p})) = \sum_{\langle ij\rangle} h_{ij}$. Consider a local part of the spin-helix state with wavevector $\mathbf{Q}_\mathrm{p}$, specifically on a pair of neighbouring spins i and j:

$$\begin{aligned} |\psi\rangle_{ij} &= \mathrm{e}^{-\mathrm{i}\Phi_i S_i^z} \mathrm{e}^{-\mathrm{i}\theta S_i^y} |S\rangle_i \otimes \mathrm{e}^{-\mathrm{i}\Phi_j S_j^z} \mathrm{e}^{-\mathrm{i}\theta S_j^y} |S\rangle_j \\ &= \mathrm{e}^{-\mathrm{i}\Phi_i (S_i^z + S_j^z)} \left(\mathrm{e}^{-\mathrm{i}\theta S_i^y} |S\rangle_i \otimes \mathrm{e}^{-\mathrm{i}\delta\Phi_{ji} S_j^z} \mathrm{e}^{-\mathrm{i}\theta S_j^y} |S\rangle_j\right), \end{aligned} \tag{15}$$

where $\Phi_i = \mathbf{Q}\cdot\mathbf{r}_i$ and $\delta\Phi_{ji} = (\Phi_j - \Phi_i)$. A simple but key property is that, for the set-ups described in either theorem, $\mathrm{e}^{-\mathrm{i}\delta\Phi_{ji}} = \mathrm{e}^{-\mathrm{i}Q_\mathrm{p}}$ or $\mathrm{e}^{\mathrm{i}Q_\mathrm{p}}$ for any nearest-neighbour pair of sites. (Clearly this is true for any hypercubic lattice. For the triangle lattice with primitive vectors $\mathbf{b}_1 = (1,0)$ and $\mathbf{b}_2 = (1/2, \sqrt{3}/2)$, we have $\mathrm{e}^{\pm\mathrm{i}4\pi/3} = \mathrm{e}^{\mp\mathrm{i}Q_\mathrm{p}}$. For the kagome lattice, the primitive vectors are $\mathbf{b}_1 = (2,0)$ and $\mathbf{b}_2 = (1, \sqrt{3})$ while the lattice vectors within each unit cell are $\mathbf{a}_1 = \frac{1}{2}\mathbf{b}_1$ and $\mathbf{a}_2 = \frac{1}{2}\mathbf{b}_2$, so the result is the same as for the triangular lattice.)

With this in mind, we evaluate the action of h_{ij} on the state

$$\begin{aligned} &\mathrm{e}^{-\mathrm{i}\Phi_i (S_i^z + S_j^z)} (S_i^x S_j^x + S_i^y S_j^y + \cos(Q_\mathrm{p}) S_i^z S_j^z) \\ &\left[\mathrm{e}^{-\mathrm{i}\theta S_i^y} |S\rangle_i \otimes \mathrm{e}^{\mp\mathrm{i}Q_\mathrm{p} S_j^z} \mathrm{e}^{-\mathrm{i}\theta S_j^y} |S\rangle_j\right] \\ = \; &\mathrm{e}^{-\mathrm{i}\Phi_i (S_i^z + S_j^z)} \mathrm{e}^{\mp\mathrm{i}Q_\mathrm{p} S_j^z} \\ &\times \left(S_i^x (S_j^x \cos(Q_\mathrm{p}) \mp S_j^y \sin(Q_\mathrm{p})) + S_i^y (S_j^y \cos(Q_\mathrm{p}) \pm S_j^x \sin(Q_\mathrm{p})) + \cos(Q_\mathrm{p}) S_i^z S_j^z\right) \\ &\times \left[\mathrm{e}^{-\mathrm{i}\theta S_i^y} |S\rangle_i \otimes \mathrm{e}^{-\mathrm{i}\theta S_j^y} |S\rangle_j\right] \\ = \; &\mathrm{e}^{-\mathrm{i}\Phi_i (S_i^z + S_j^z)} \mathrm{e}^{\mp\mathrm{i}Q_\mathrm{p} S_j^z} \\ &\times \left(\cos(Q_\mathrm{p})(S_i^x S_j^x + S_i^y S_j^y + S_i^z S_j^z) \mp \sin(Q_\mathrm{p})(S_i^x S_j^y - S_i^y S_j^x)\right) \\ &\times \left[\mathrm{e}^{-\mathrm{i}\theta S_i^y} |S\rangle_i \otimes \mathrm{e}^{-\mathrm{i}\theta S_j^y} |S\rangle_j\right]. \end{aligned} \tag{16}$$

The term proportional to $\cos(Q_\mathrm{p})$ is $\mathbf{S}_i\cdot\mathbf{S}_j$, and the state on the right-hand side of the last line of the above equation is a uniformly polarized state, so it evaluates to the original state up to a multiplicative factor

$$S^2 \cos(Q_\mathrm{p}) |\psi\rangle_{ij}. \tag{17}$$

Now we just have to evaluate the term proportional to $\sin(Q_\mathrm{p})$. Ignoring the factor $\mathrm{e}^{-\mathrm{i}\Phi_i (S_i^z + S_j^z)} \mathrm{e}^{\mp\mathrm{i}Q_\mathrm{p} S_j^z}$, we have

$$\begin{aligned} &\mp \sin(Q_\mathrm{p})(S_i^x S_j^y - S_i^y S_j^x) \left[\mathrm{e}^{-\mathrm{i}\theta S_i^y} |S\rangle_i \otimes \mathrm{e}^{-\mathrm{i}\theta S_j^y} |S\rangle_j\right] \\ = \; &\mp \sin(Q_\mathrm{p})(\mathrm{e}^{-\mathrm{i}\theta S_i^y} \mathrm{e}^{-\mathrm{i}\theta S_j^y}) \\ &\times \left[(S_i^x \cos(\theta) + S_i^z \sin(\theta)) S_j^y - S_i^y (S_j^x \cos(\theta) + S_j^z \sin(\theta))\right] \\ &\times |S\rangle_i \otimes |S\rangle_j \\ = \; &\mp \sin(Q_\mathrm{p})(\mathrm{e}^{-\mathrm{i}\theta S_i^y} \mathrm{e}^{-\mathrm{i}\theta S_j^y}) \\ &\times \left[\cos(\theta)\,(S_i^x S_j^y - S_i^y S_j^x) + \sin(\theta)\, S(S_j^y - S_i^y)\right] \\ &\times |S\rangle_i \otimes |S\rangle_j\,. \end{aligned} \tag{18}$$

Now we make use of the fact that

$$S_i^y\,|S\rangle_i = \mathrm{i}S_i^x\,|S\rangle_i \tag{19}$$

(this follows from the definition of $|S\rangle_i$ as the highest-weight state, $S_i^x = \frac{1}{2}(S_i^+ + S_i^-)$, and $S_i^y = \frac{1}{2\mathrm{i}}(S_i^+ - S_i^-)$). Therefore

$$(S_i^xS_j^y - S_i^yS_j^x)\,|S\rangle_i\,|S\rangle_j = 0 \tag{20}$$

and equation (18) becomes

$$\mp\sin(Q_\mathrm{p})\,\mathrm{e}^{-\mathrm{i}\theta S_i^y}\mathrm{e}^{-\mathrm{i}\theta S_j^y}\,\mathrm{i}\sin(\theta)\,S(S_j^x - S_i^x)\,|S\rangle_i\,|S\rangle_j\,. \tag{21}$$

We add a trivial term

$$\mp\sin(Q_\mathrm{p})\,\mathrm{e}^{-\mathrm{i}\theta S_i^y}\mathrm{e}^{-\mathrm{i}\theta S_j^y}\,\mathrm{i}\cos(\theta)\,S(S_j^z - S_i^z)\,|S\rangle_i\,|S\rangle_j \tag{22}$$

to it, so that equation (18) is equal to

$$\pm\mathrm{i}S\sin(Q_\mathrm{p})(S_j^z - S_i^z)\,\mathrm{e}^{-\mathrm{i}\theta S_i^y}\mathrm{e}^{-\mathrm{i}\theta S_j^y}\,|S\rangle_i\,|S\rangle_j\,. \tag{23}$$

Reinstating the factor $\mathrm{e}^{-\mathrm{i}\Phi_i(S_i^z+S_j^z)}\mathrm{e}^{\mp\mathrm{i}Q_\mathrm{p}S_j^z}$ which commutes with $(S_j^z - S_i^z)$, we hence have

$$h_{ij}|\psi\rangle_{ij} = S^2\cos(Q_\mathrm{p})|\psi\rangle_{ij} \pm \mathrm{i}S\sin(Q_\mathrm{p})\left(S_j^z - S_i^z\right)|\psi\rangle_{ij}. \tag{24}$$

This is our final result. The $(S_i^z - S_j^z)$ term cancels out in the bulk when summed over all sites (it telescopes), so

$$H(\cos(Q_\mathrm{p}))\,\left|\psi(\mathbf{Q}_\mathrm{p})\right\rangle = (S^2\cos(Q_\mathrm{p}) \times \#\mathrm{Links})\,\left|\psi(\mathbf{Q}_\mathrm{p})\right\rangle \tag{25}$$

as claimed.

Lastly, we discuss the physical implications of these results. The more general spin systems considered here are expected to be non-integrable, and so now these phantom helices constitute exceptional initial states that do not thermalize. That is, they are examples of quantum many-body scars, first discussed in the context of a Rydberg atom array[55], where a special Neél configuration of spins exhibited anomalously long-lived many-body revivals. In our present case, the helix states can be made to display similar phenomenology by considering them outside the rotating frame. They are no longer exact many-body eigenstates due to the extra global Zeeman term and acquire dynamics consisting of coherent, perfect many-body revivals.

Experimental protocol for phantom helix states in two dimensions. Our experimental protocol can be extended to two (or three) spatial dimensions to directly observe higher-dimensional phantom helices and the associated quantum scarred dynamics. The protocol includes:

1. Prepare atoms deep in a Mott insulator state.
2. Wind a spin helix with an arbitrary $\mathbf{Q}=(Q_x, Q_y, Q_z)$ vector by applying a magnetic field gradient in the direction of $\mathbf{Q}$.
3. Enable spin dynamics in two (or three) spatial dimension by reducing the lattice depth of two (or three) lattice beams. After an evolution time t, freeze the dynamics again by rapidly increasing the lattice depth.
4. Unwind the spin modulation to a resolvable wavevector $\mathbf{Q}_\mathrm{measure}$ which is also perpendicular to the imaging axis. This allows measuring the contrast of spin helices with any wavevector $\mathbf{Q}$, without adjusting the imaging axis each time.
5. Image the spin modulation to measure the contrast.

A possible technical challenge is the switching of high magnetic fields. Many atoms, including 7Li, have Feshbach resonances at high bias fields, which can usually be created only along one specific direction. Any added gradient is projected along the strong bias field. Therefore, to apply gradients in arbitrary directions, the high magnetic field has to be switched off, and additional small coils can then provide a low bias field in any direction.

For ^{7}Li, the Mott insulator condition is best met at high field. Furthermore, the polarization-rotation imaging technique[16] works best at high fields. Therefore, the extension of our experiment to studies of phantom states in higher dimensions requires a protocol with three steps at high field, interlaced with steps at low field. In the 1D experiment, all steps could be done at high field.

During the field ramps, the atoms must be isolated, that is, stay in a Mott insulator state. However, during the magnetic field ramp, the atomic scattering lengths will change. If this involves small scattering lengths, the lattice depth must be increased. ^{7}Li atoms have very small scattering lengths at low fields (smaller than a few Bohr radii a_0) and would require lattice depths of at least $70E_R$, which requires very high laser power due to the light mass and therefore large recoil energy of ^{7}Li.

Extended Hubbard model. For small scattering lengths $a_{\uparrow\uparrow}$, $a_{\uparrow\downarrow}$, $a_{\downarrow\downarrow} \ll a_\mathrm{osc}$~1,000$a_0$ (that is, far from any Feshbach resonances), the mapping from the Bose–Hubbard model to a spin Hamiltonian is well understood. We use this regime to compare the values of Δ obtained from the minimum of the observed decay rate and the phantom condition versus the predictions of the microscopic model. This validates the phantom phenomenon as a protocol to determine the anisotropy Δ. For the needed accuracy, we must add corrections to the most basic superexchange model of equation (4). Those corrections can be found in ref. [30] and in the Methods section of ref. [16] and are summarized here.

The standard Hubbard model in the single-band approximation is fully parameterized by the tunnelling matrix element $\tilde{t}^{(0)}$ and the on-site interaction $U_{\sigma\sigma'}^{(0)}$ and is almost exactly realized with cold atoms in optical lattices. These parameters can be calculated using the lowest-band Wannier functions $w(\mathbf{r})=w_x(x)w_y(y)w_z(z)$ along each lattice depth using the expressions

$$\tilde{t}^{(0)} = -\int \mathrm{d}z\,w_z(z-a)\left[-\frac{\hbar^2}{2m}\frac{\mathrm{d}^2}{\mathrm{d}z^2} + V_0\sin^2(kz)\right]w_z(z) \tag{26}$$

and

$$U_{\sigma\sigma'}^{(0)} = g_{\sigma\sigma'}\int \mathrm{d}^3r\,|w(\mathbf{r})|^4, \tag{27}$$

where $\sigma, \sigma' \in \{\uparrow, \downarrow\}$, $g_{\sigma\sigma'} = 4\pi\hbar^2 a_{\sigma\sigma'}/m$ and $k=\pi/a$ is the wavevector of the lattice. The standard Hubbard model results in the spin-independent tunnelling parameter $\tilde{t}^{(0)} \to \tilde{t}$ that is used in equation (4). The three largest corrections to the standard superexchange model correspond to bond-charge tunnelling, higher-order bands and off-site contact interactions.

Correction 1. The largest correction to tunnelling is the so-called bond-charge tunnelling term, which for an $n=1$ Mott insulator is[30,32]

$$\tilde{t}_{\sigma\sigma'}^{(1)} = -g_{\sigma\sigma'}\int \mathrm{d}^3r\,w^*(\mathbf{r}-\delta\mathbf{r})w^*(\mathbf{r})w(\mathbf{r})w(\mathbf{r}). \tag{28}$$

where $\delta\mathbf{r}=(0,0,a)$. Note that this correction, unlike $\tilde{t}^{(0)}$, is spin dependent. Even far from the Feshbach resonance, this term results in a correction to the calculated Δ.

Correction 2. Using second-order perturbation theory, higher-order band corrections to $U_{\sigma\sigma'}$ occur via virtual excitations to higher Wannier bands due to interactions between two atoms. Admixtures of these higher bands are, to the lowest order,

$$U_{\sigma\sigma'}^{(1)} = -\sum_{\mathbf{n}_1\mathbf{n}_2}\frac{g_{\sigma\sigma'}^2}{E_{\mathbf{n}_1\mathbf{n}_2}}\left|\int \mathrm{d}^3r\,w_{\mathbf{n}_1}^*(\mathbf{r})w_{\mathbf{n}_2}^*(\mathbf{r})w(\mathbf{r})w(\mathbf{r})\right|^2, \tag{29}$$

where $\mathbf{n}_1$ and $\mathbf{n}_2$ are the three-dimensional band indices of the two particles and $E_{\mathbf{n}_1\mathbf{n}_2}$ is the sum of the band gaps of particles in bands $\mathbf{n}_1$ and $\mathbf{n}_2$ relative to the lowest band $\mathbf{n}_0=(0,0,0)$ (ref. [16]).

Correction 3. Nearest-neighbour off-site interactions are given by the expression

$$V_{\sigma\sigma'} = g_{\sigma\sigma'}\int \mathrm{d}^3r\,w^*(\mathbf{r}-\delta\mathbf{r})w^*(\mathbf{r})w(\mathbf{r}-\delta\mathbf{r})w(\mathbf{r}). \tag{30}$$

For a Mott insulator state, the spin physics is still described by a Heisenberg model with modified parameters in equation (4) (see next section)

$$\begin{aligned} J_z &= (4\tilde{t}_{\uparrow\downarrow}^2/U_{\uparrow\downarrow} - 4V_{\uparrow\downarrow}) - (4\tilde{t}_{\downarrow\downarrow}^2/U_{\downarrow\downarrow} - 2V_{\downarrow\downarrow}) - (4\tilde{t}_{\uparrow\uparrow}^2/U_{\uparrow\uparrow} - 2V_{\uparrow\uparrow}) \\ J_{xy} &= -4\tilde{t}_{\uparrow\downarrow}^2/U_{\uparrow\downarrow}, \end{aligned} \tag{31}$$

where $\tilde{t}_{\sigma\sigma'} = \tilde{t}^{(0)} + \tilde{t}_{\sigma\sigma'}^{(1)}$ and $U_{\sigma\sigma'} = U_{\sigma\sigma'}^{(0)} + U_{\sigma\sigma'}^{(1)}$. Next-order corrections such as correlated-pair tunnelling and corrections to on-site energies due to next-nearest-neighbour interactions[30] are two and four orders of magnitude smaller than bond-charge tunnelling $\tilde{t}_{\sigma\sigma'}^{(1)}$ and nearest-neighbour off-site interactions $V_{\sigma\sigma'}$, respectively, and therefore not included in our analysis.

We now discuss the physical origin of the strong variation of Δ observed near Feshbach resonance (Fig. 5). Near a Feshbach resonance, the interaction term $g_{\sigma\sigma'} \propto a_{\sigma\sigma'}$ becomes large. However, the contribution via U to the spin interactions is small due to the $(\tilde{t}^{(0)})^2/U_{\sigma\sigma'}^{(0)} \propto 1/a_{\sigma\sigma'}$ dependence of the spin interactions. In contrast, both the bond-charge tunnelling and the off-site corrections increase $\propto a_{\sigma\sigma'}$ and provide corrections to the spin interactions $\propto a_{\sigma\sigma'}$. However, due to the signs in equation (31), near a ↑↑ Feshbach resonance, the bond-charge terms are proportional to $-a_{\uparrow\uparrow}$ while the off-site terms are proportional to $+a_{\uparrow\uparrow}$ and therefore have the opposite dispersive shape when plotted versus magnetic field. Calculations based on equation (31) show that the off-site terms dominate, in agreement with the experimentally observed dispersive shape in Fig. 5. Note that the two ↑↑ Feshbach resonances in Fig. 5 have the same dispersive shape, as can be seen in Fig. 3 of ref. [23]. Also, note that higher-order band corrections slightly modify the magnitude of the superexchange and bond-charge contributions by replacing the denominator $U_{\sigma\sigma'}^{(0)} \to U_{\sigma\sigma'}^{(0)} + U_{\sigma\sigma'}^{(1)}$ but have very little effect on their scaling with $a_{\uparrow\uparrow}$.

Therefore, we conclude that only the off-site interactions in equation (30) have the correct 'symmetry' to qualitatively explain the observed variation of Δ near the two Feshbach resonances in Fig. 5.

General nearest-neighbour spin-1/2 model in 1D. Here we discuss under which assumptions an extended Bose–Hubbard model effectively realizes a Heisenberg XXZ Hamiltonian in the Mott insulating regime. For ultracold atoms, the underlying Bose–Hubbard model, even near Feshbach resonances, is formulated as a nearest-neighbour model. That is, direct next-nearest-neighbour interactions and direct tunnelling between non-neighbouring sites are neglected.

Deep in the Mott insulator regime near unity filling and assuming a two-component system, charge transport is suppressed, and the only remaining dynamics is that of spin degrees of freedom.

The effective spin model is then also nearest neighbour in nature, and furthermore conserves the total S^z component (that is, the number of bosons in each hyperfine state). This has the following general form

$$H=\sum_{\langle ij\rangle}[J_1(S_i^xS_j^x+S_i^yS_j^y)+J_2(S_i^xS_j^y-S_i^yS_j^x)+J_zS_i^zS_j^z+g_iS_i^z+g_jS_j^z]. \quad (32)$$

The term parameterized by J_2 represents a Dzyaloshinskii–Moriya term and breaks time-reversal symmetry since it is odd under complex conjugation. Therefore, under the additional assumption that the underlying Bose–Hubbard model is time-reversal invariant, the most general spin model must be the XXZ Hamiltonian, with the possible addition of effective local magnetic fields S_i^z. Breaking of time-reversal invariance would require a complex hopping matrix element, that is a Peierl's phase, usually introduced by spin–orbit coupling or Floquet-type time modulation of the lattice.

Non-integrable long-range spin-1/2 model in 1D. The existence of phantom states in higher dimensions demonstrates that integrability is not necessary for their stability. This raises the question of what would happen in 1D if additional interactions were added to the nearest-neighbour spin-1/2 XXZ Hamiltonian. Here, we present a model where integrability is broken through the addition of long-range interactions, while still retaining the phantom spiral with wavevector Q_p as a quantum many-body eigenstate. This elevates the phantom spiral to a genuine quantum many-body scar even in 1D.

We consider the Hamiltonian

$$H=\sum_{n>0}J_n\sum_i[S_i^xS_{i+n}^x+S_i^yS_{i+n}^y+\Delta_nS_i^zS_{i+n}^z], \quad (33)$$

where J_n are arbitrary amplitudes and Δ_n is the anisotropy associated with each n, which is a general long-range Heisenberg XXZ model. (Note that the model considered in the paper is specified by $J_1\neq0, J_{n\neq1}=0$ and $\Delta_1=\Delta=\cos(Q_\mathrm{p})$. We set the lattice spacing to $a=1$ for brevity.) Now, if $\Delta_n=\cos(nQ_\mathrm{p})$ for all n, the phantom spiral with wavevector Q_p will again be an exact eigenstate of the Hamiltonian, assuming an infinite lattice. The proof follows mutatis mutandis the one in the paper. For a finite lattice, it will be a metastable state due to the effect of boundary terms which break the exact solvability. While we note that this Hamiltonian would be extremely difficult to realize experimentally because Δ_n for each distance n must be fine-tuned, it does however provide an illustrative example of a deformation to the original Heisenberg Hamiltonian that preserves the phantom helix as an eigenstate of the system while breaking integrability.

We can show that the presence of longer-range interactions renders the model non-integrable by numerically computing the model's level-spacing statistics. Specifically, we resolve all global symmetries of the system and compute the level-spacing ratio $r_n=\frac{\min(\delta E_n,\delta E_{n+1})}{\max(\delta E_n,\delta E_{n+1})}\in[0,1]$ where $\delta E_n=E_{n+1}-E_n$ and E_n is the ordered list of many-body energies[56]. In Extended Data Fig. 5, we plot the average r value, $\langle r\rangle$, for the model with parameters $J_1=1$, $J_{n>2}=0$, $\Delta_n=\cos(nQ_\mathrm{p})$ and variable J_2. As can be seen, for the Hamiltonian with purely nearest-neighbour interactions ($J_2=0$), one gets $\langle r\rangle\approx0.39$, consistent with the Poissonian statistics expected of an integrable system. In contrast, in the presence of next-nearest-neighbour interactions ($J_2\neq0$), $\langle r\rangle\approx0.53$ for large enough J_2, consistent with Wigner–Dyson statistics in the Gaussian orthogonal ensemble, indicating that the model is non-integrable.

Data availability

The data that support the findings of this study are available from the corresponding author upon reasonable request.

Code availability

The code that supports the findings of this study is available from the corresponding author upon reasonable request.

References

54. Dimitrova, I. et al. Enhanced superexchange in a tilted mott insulator. *Phys. Rev. Lett.* **124**, 043204 (2020).
55. Bernien, H. et al. Probing many-body dynamics on a 51-atom quantum simulator. *Nature* **551**, 579–584 (2017).
56. Oganesyan, V. et al. Localization of interacting fermions at high temperature. *Phys. Rev. B* **75**, 155111 (2007).

Acknowledgements

We thank J. Rodriguez-Nieva for helpful discussions and J. Amato-Grill for important advice. We thank J. Xiang for experimental assistance, J. de Hond for comments on the manuscript and M. Zwierlein for sharing equipment. We acknowledge support from the NSF through the Center for Ultracold Atoms and grant no. 1506369, the Vannevar-Bush Faculty Fellowship and DARPA (grant no. W911NF2010090). W.W.H. is supported in part by the Stanford Institute of Theoretical Physics. Y.K.E.L. is supported in part by the National Science Foundation Graduate Research Fellowship under grant no. 1745302.

Author contributions

P.N.J., Y.K.E.L., H.L., W.W.H. and W.K. conceived the experiment. P.N.J., Y.K.E.L., H.L., I.D. and Y.M. performed the experiment. P.N.J., Y.K.E.L. and H.L. analysed the data. W.W.H. generalized the findings to higher dimensions. All authors discussed the results and contributed to the writing of the manuscript.

Competing interests

The authors declare no competing interests.

Additional information

Extended data is available for this paper at https://doi.org/10.1038/s41567-022-01651-7.

Correspondence and requests for materials should be addressed to Yoo Kyung 'Eunice' Lee.

Peer review information *Nature Physics* thanks the anonymous reviewers for their contribution to the peer review of this work.

Reprints and permissions information is available at www.nature.com/reprints.

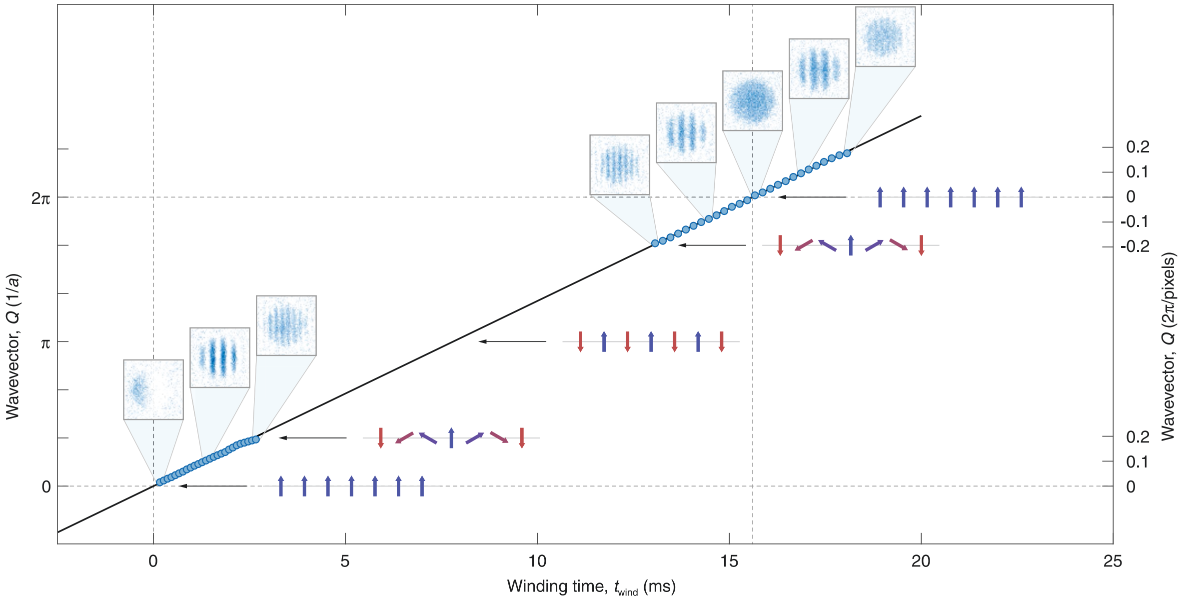

Extended Data Fig. 1 | Calibration of the wavevector *Q*. Starting with all spin aligned, under a constant magnetic field gradient B', the wavevector Q grows linearly starting from 0 as a function of winding time t_{wind} until at time $t_{\text{wind}} = T = 15.608(4)$ ms we reach a wavevector $Q = 2\pi/a$ and all spins are aligned again. All observed wavevectors fall on a line which determines the magnetic field gradient as $\mu B'/\hbar = (2\pi/a)/T = 2\pi \times 64.068(15)$ Hz/a at a bias field of $B = 882.612$ G. The error bar of T implies an uncertainty in Q of at most $\pm 0.001 \times 2\pi/a$.

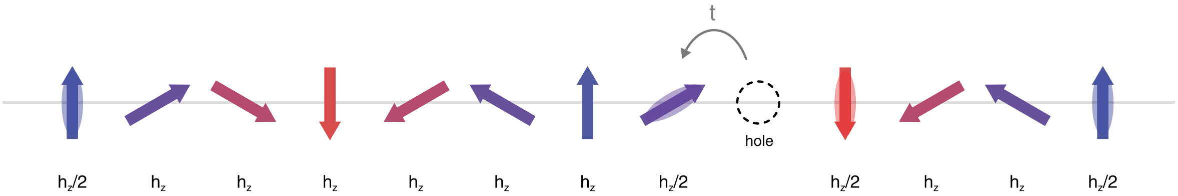

Extended Data Fig. 2 | Dephasing at the chain ends and holes. If a spin has only *one* nearest neighbour, it experiences a torque and dephases rapidly at a rate ~J_{xy} (as opposed to a spin with *two* nearest neighbours, whose interactions cancel exactly in a phantom helix). This is the case for the spins at the two ends of the spin chain, as well as next to a hole. Additionally, the same spins experience an effective magnetic field $h_z = 4\tilde{t}^2/U_{\uparrow\uparrow} - 4\tilde{t}^2/U_{\downarrow\downarrow}$ (created by superexchange), which is reduced by a factor of two, compared to the bulk. This modifies the boundary condition at the ends, and can lead to dephasing.

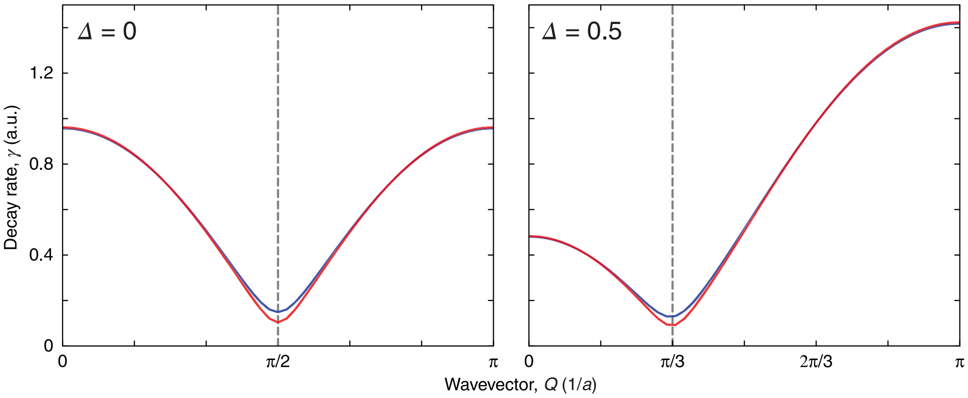

Extended Data Fig. 3 | Numerically calculated contrast decay of finite, open chains. The simulation is performed using spin chains with 8 sites (blue) and 15 sites (red), for $\Delta = 0$ (left) and 0.5 (right). The decay rate $\gamma(Q)$ is determined using a short-time quadratic expansion as derived in ref. [17]. The open chain boundary condition introduces a finite contrast decay even when the phantom condition is met (dashed line), but does not shift the Q-value at which the minimum decay rate occurs.

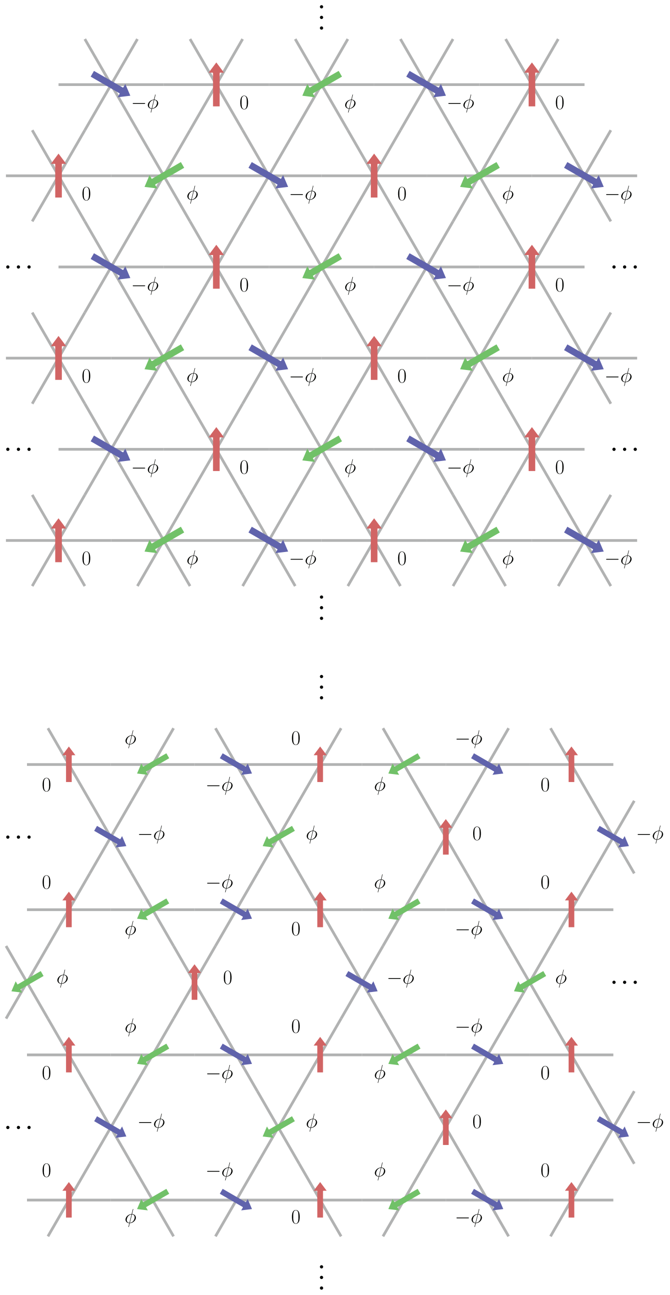

Extended Data Fig. 4 | Phantom spin helices for triangular and kagome lattices. As in the case of the square lattice (see Fig. 4), we label each vertex with its azimuthal angle in the transverse plane. However, in the case of a triangular lattice (top) or kagome lattice (bottom), only $\phi = Q_p = \pm 2\pi/3$ and $\Delta = -1/2$ defines a valid phantom spin helix. Thus, the spin can only point in one of three directions in the S^x-S^y plane (denoted by three different colours), with relative angle $2\pi/3$ between them. Note that the colinear neighbours of each red spin are blue and green spins, and the interactions of the blue and green spins with the red spin cancel for each line. In this way, one can understand the 2D phantom helix states as arising from simple 'stacking' together of phantom helices of 1D chains.

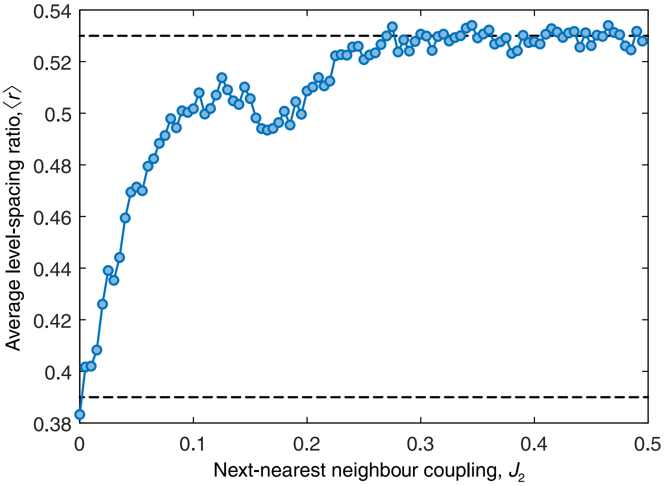

Extended Data Fig. 5 | Level spacing statistics for the extended spin-1/2 XXZ model. The model is defined by equation (33) with $J_1=1$, $J_{n>2}=0$, $\Delta_n = \cos(nQ_p)$, and variable J_2. We numerically simulate a system of $N=22$ spins on a ring, and choose $Q_\mathrm{p}=2\pi m/N$ where $m=3$, which gives $\Delta_1\approx0.654$ and $\Delta_2\approx-0.142$. The spin helix with wavevector Q_p can be proven to be an exact quantum many-body eigenstate for any J_2. We resolve global symmetries and compute eigenvalues in the sector with momentum $k=0$, spin-flip $G=1$, reflection parity $R=1$, and magnetization $M=0$. As can be seen, at $J_2=0$ the average r-parameter $\langle r\rangle\approx0.39$ (bottom dashed line), consistent with Poissonian statistics indicating an integrable system. When $J_2\neq0$, $\langle r\rangle\rightarrow0.53$ (top dashed line) for large enough J_2, consistent with Wigner-Dyson statistics in the Gaussian Orthogonal Ensemble (GOE), indicating that integrability has been broken. We expect the behaviour of $\langle r\rangle$ at $J_2=0$ to be singular in the limit of very large system sizes; that is, any infinitesimal perturbation J_2 in the thermodynamic limit will be sufficient to render the model non-integrable.